PHILOSOPHICAL TRANSACTIONS A

rsta.royalsocietypublishing.org

Research

Cite this article: Nandi TN, Herrig A, Brasseur JG. 2017 Non-steady wind turbine response to daytime atmospheric turbulence. *Phil. Trans. R. Soc. A* **375**: 20160103.
http://dx.doi.org/10.1098/rsta.2016.0103

Accepted: 3 January 2017

One contribution of 11 to a theme issue 'Wind energy in complex terrains'.

Subject Areas:
mechanical engineering, power and energy systems, energy, fluid mechanics

Keywords:
field experiment, atmospheric turbulence, large-eddy simulation, actuator line methodology

Author for correspondence:
James G. Brasseur
e-mail: brasseur@colorado.edu

Non-steady wind turbine response to daytime atmospheric turbulence

Tarak N. Nandi[1], Andreas Herrig[2] and James G. Brasseur[1,3]

[1]Department of Mechanical and Nuclear Engineering, Pennsylvania State University, University Park, PA 16802, USA
[2]Aerodynamics and Acoustics Lab, GE Global Research, Munich, 85748 Garching bei Muenchen, Germany
[3]Department of Aerospace Engineering Sciences, University of Colorado, Boulder, CO 80302, USA

JGB, 0000-0002-3007-4276

Relevant to drivetrain bearing fatigue failures, we analyse non-steady wind turbine responses from interactions between energy-dominant daytime atmospheric turbulence eddies and the rotating blades of a GE 1.5 MW wind turbine using a unique dataset from a GE field experiment and computer simulation. Time-resolved local velocity data were collected at the leading and trailing edges of an instrumented blade together with generator power, revolutions per minute, pitch and yaw. Wind velocity and temperature were measured upwind on a meteorological tower. The stability state and other atmospheric conditions during the field experiment were replicated with a large-eddy simulation in which was embedded a GE 1.5 MW wind turbine rotor modelled with an advanced actuator line method. Both datasets identify three important response time scales: advective passage of energy-dominant eddies ($\approx$ 25–50 s), blade rotation (once per revolution (1P), $\approx$ 3 s) and sub-1P scale ($<$ 1 s) response to internal eddy structure. Large-amplitude short-time ramp-like and oscillatory load fluctuations result in response to temporal changes in velocity vector inclination in the aerofoil plane, modulated by eddy passage at longer time scales. Generator power responds strongly to large-eddy wind modulations. We show that internal dynamics of the blade boundary layer near the trailing edge is temporally modulated by the non-steady

THE ROYAL SOCIETY PUBLISHING

external flow that was measured at the leading edge, as well as blade-generated turbulence motions.

This article is part of the themed issue 'Wind energy in complex terrains'.

1. Introduction

Modern commercial utility-scale wind turbines operate in the lower 10–15% of the atmospheric boundary layer (ABL) and experience temporally and spatially varying inflow from coherent ABL turbulence structures during the daytime that results from the interaction between surface layer mean shear and buoyancy-driven thermal motions [1]. The interactions of the rotating wind turbine blades with the energy-dominant ABL turbulence eddies cause temporal and spatial variations in the blade boundary layer structure [2]. In particular, the passage of coherent energetic turbulence eddies through the rotor disc lead to large time variations in local surface stresses on the turbine blades. These blade–ABL eddy interactions underlie the observed large transients in a variety of loadings important for wind turbine function and undermine reliability [3]. Wind turbine components suffer from fatigue loading due to the inherent non-steady nature of the ABL inflow, which has fluctuations with length and time scales spanning multiple orders of magnitude.

This study combines a unique field experiment carried out by GE with high-fidelity computer simulations to develop detailed understanding of the non-steady responses in wind turbine blade loadings due to aerodynamic forcings on rotating blades during the passage of energy-dominant daytime ABL turbulence eddies through the rotor plane. Other field campaigns focusing on the influence of ABL turbulence on the non-steady response of utility-scale wind turbines include the experiments at University of Minnesota [4,5], the DAN-AERO experiment in Denmark [6] and experiments at the NREL National Wind Technology Center in Colorado, USA [7].

Levelized cost of energy (LCOE) and wind farm profitability are both significantly reduced by the failures of drivetrain components on significant numbers of wind turbines in wind farms. Historically, it is well known that premature gearbox failures are a major source of operation and maintenance cost and lost profitability, and research has pointed to the bearings as the main failure points [8]. It is now understood that bearing failures are largely driven by the non-steady stresses experienced by the components from aerodynamic forcings by inflow turbulence [9]. Anecdotal information (private communication at the recent Drivetrain Reliability Collaborative Workshop at NREL on 16–17 February 2016 between several wind farm developers and J.G.B.) suggests that premature failure of the main bearings is another major contributor to reduced LCOE and wind farm profitability, with direct roots in the non-steady changes in moments on the low-speed shaft [10]. This study focuses on non-steady loadings driven by the interactions between the more energetic turbulence eddies in the daytime ABL and the wind turbine rotor that underlie non-steady moments entering the drivetrain at the hub. This study is therefore of primary relevance to the wind turbines directly responding to atmospheric turbulence in the first few rows of a wind farm. Farther into the wind farm, rotor wake turbulence, modulated by atmospheric turbulence, contributes to non-steady loadings.

Previous studies have shown that the stability state of the lower troposphere (the ABL) has a major impact on the coherent structure of the turbulence eddies [1], with corresponding differences in wind turbine loading response [11,12]. The daytime ABL in the continental USA and Europe is globally unstable (convective) due to solar heating of the ground. Wind turbines typically operate in winds of moderate strength, so that the turbulence structure of the ABL is created by a mix of shear production near the ground and buoyancy production in the mixed layer above, the essential character of a 'moderately convective' atmospheric boundary layer (MCBL) [1,13,14]. In this study, we combine time-resolved aerodynamic data measured locally at three outer blade sections on a GE 1.5 MW wind turbine blade and high-frequency SCADA generator power data from a daytime field campaign in northern Germany with a computer

simulation that mimics the GE wind turbine in a high-resolution large-eddy simulation (LES) of a close approximation of the atmospheric turbulence experienced by the wind turbine in the field campaign. To estimate the stability state of the ABL experienced by the GE wind turbine in the field, use was made of time-resolved meteorological data measured on an upwind meteorological tower (met. tower) and meteorological data from a nearby airport. The sectional load responses of the GE wind turbine blades were modelled using an advanced actuator line method [12,15] with lift/drag polars supplied by GE. By combining the experimental and numerical datasets, we describe time-response characteristics of the local loadings on the blade sections in response to non-steady non-uniform energetic atmospheric turbulence eddies within a daytime ABL which have spatial scale commensurate with the turbine blade length [2,16].

2. The 1.5 MW GE wind turbine field experiment

In this paper, we analyse a unique dataset from a field campaign carried out at a GE test site in northwestern Germany. These data are proprietary to GE and are analysed in the public domain for the first time in this study. Data were collected for 19 different runs (of varying durations ranging from 4 min to 81 min) spanning 11 days from July to September 2008. The terrain around the wind turbine was overall flat, but a water channel bounded by two rows of low-lying trees ($\lesssim$ 10 m high) was present approximately 310 m upwind of the wind turbine. A met. tower was placed approximately 250 m upwind of the 1.5 MW wind turbine in the prevailing wind direction. Figure 1 is a schematic of the met. tower and the wind turbine. The turbine had a rotor diameter of 77 m and the hub was at a height of 80 m from the ground. The instrumentation of the met. tower is described in §2a.

One of the three blades was instrumented with leading-edge five-hole probes (LE probes) and trailing-edge pitot rakes (TE rakes) to collect rotor inflow and trailing-edge boundary layer data. Generator power was obtained from the SCADA system. This instrumentation is described in §2b.

(a) Meteorological tower instrumentation and data

The details of the data used from the met. tower instrumentation are provided in table 1. As illustrated in figure 1, wind speed was measured by cup anemometers at three heights, and recorded at 16 Hz (downsampled from 16 384 Hz). A sonic anemometer measured three velocity components near hub height at 1 Hz. Wind direction was measured at two heights at 16 Hz and temperature at two heights (16 Hz) in addition to the sonic (1 Hz).

(b) Wind turbine instrumentation and data

From the high-speed shaft, generator revolutions per minute (r.p.m.) and electrical power output data were available indirectly. The power obtained from the SCADA system was measured via a Woodward MFR13 industry-grade protective multifunction relay with true RMS voltage and current sensing, low-pass filtered at 200 Hz (well above the highest frequencies of interest and satisfying the Nyquist dealiasing criterion). The analogue outputs of the MFR13 were sampled by an LMS Scadas III DAQ system. R.p.m. was obtained from the controller, low-pass filtered at 5 Hz. Time-resolved angular positions of the instrumented blade were measured by an encoder from which blade r.p.m. was obtained and used to validate generator r.p.m. through the gear ratio. The SCADA system also supplied time-resolved blade pitch angle. One of the three blades was specially instrumented with leading-edge five-hole probes and trailing-edge rakes at three radial locations (referred to as inboard, midboard and outboard hereafter), as described in table 2 and shown in figure 2. These sensors were custom-made by Aeroprobe Inc. to meet the design specifications provided by GE, and were offset radially to reduce the possibility of leading-edge probe influence on the corresponding trailing-edge rake.

The tip of the inboard and midboard five-hole probes was 1150 mm from the blade leading edge, and that of the outboard probe was 850 mm from the leading edge. Five-hole probe heads

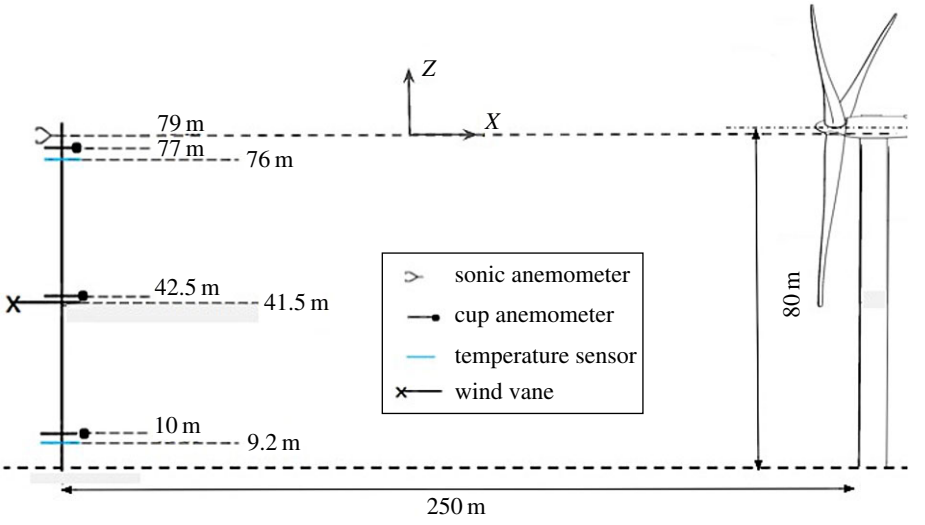

Figure 1. Schematic of the instrumented meteorological tower and the wind turbine. (Online version in colour.)

Table 1. Meteorological tower instrumentation.

measured quantity	height	instrument	storage frequency
wind velocity	10 m, 42.5 m, 77 m	Thies first class cup anemometer	16 Hz
	79 m	3D Metec sonic anemometer	1 Hz
wind direction	41.5 m	wind vane	16 Hz
	79 m	3D Metec sonic anemometer	1 Hz
temperature	9.2 m, 76 m	Thies temperature sensor	16 Hz
	79 m	3D Metec sonic anemometer	1 Hz

Table 2. Wind turbine blade instrumentation.

sensor	approx. radial locations (% blade length)	derived quantities	storage frequency
leading-edge five-hole pitot probes	74%, 87%, 95%	velocity components, inflow angles	16 Hz
trailing-edge pitot rakes	73%, 86%, 94%	velocity magnitude	16 Hz

of 7.94 mm outer diameter and 127 mm length made from aluminium were connected to tapered carbon-fibre probe shafts, to minimize deflections. The pitot tube pressure signals were acquired with three customized Scanivalve DSA3217 pressure scanners, with simultaneously sampling piezoresistive pressure sensor modules of 2 × 8 channels each. The static pressure was obtained using static rings located approximately 3 cm downstream of the tips of the LE probes. Stiff nylon pressure tubes of 1.6 mm outer diameter (OD), 0.79 mm inner diameter (ID) and about 0.2–0.3 m length were used to extend the probe stainless-steel tubes (with 0.76 mm ID) to the DSAs, totalling approximately 1.5 m in length. The master scanner contained internal valves to purge the pressure ports. The midboard and outboard scanners had full-scale ranges of ±5 kPa (±0.12% full-scale long-term accuracy), and the inboard ±2.5 kPa (±0.2% accuracy), allowing an accuracy of ±6 Pa and ±5 Pa, respectively.

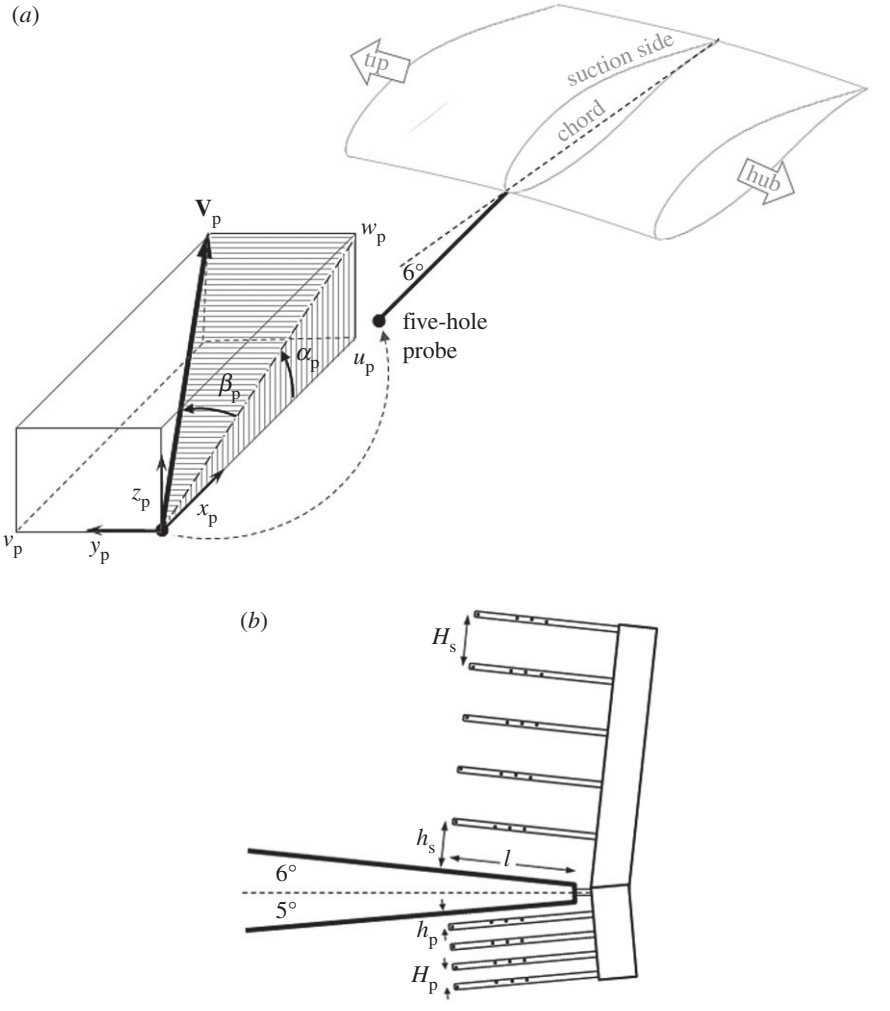

Figure 2. The GE 1.5 MW wind turbine blade instrumentation. (*a*) The leading-edge probe with the local coordinate system. The probe 'boom' makes an angle of 6° with the local chord. The velocity vector $\mathbf{V}_p$ is measured at the probe relative to the blade section. (*b*) The trailing-edge rake (suction surface at the top). Dimensions are provided in §2b.

Honeywell model DS absolute pressure sensors with 30 psia range and 0.1% full-scale accuracy for measuring the absolute static pressure on the LE probes were sampled at 400 Hz via Ethernet. Signals were transferred from hub to nacelle over an optical slip ring, and several Ethernet-connected PCs were placed in the hub and tower base to handle and store data. Time synchronization was achieved via a Meinberg IRIG-B clock generator connecting the hub and tower PCs over a galvanic slip ring.

Wind tunnel five-hole probe calibration coefficients for velocity vector components and angles α_p and β_p (figure 2*a*) were determined by fourth-order polynomial fits. Placing the DSAs close to the five-hole probes and using short tube lengths resulted in high cut-off frequency of ≈ 30 Hz (determined from acoustic calibrations, defined as the -3 dB drop-off point here), eliminating the need for frequency response corrections. In §5, we analyse the response of the flow velocity vector $\mathbf{V}_p$ to ABL turbulence.

Trailing-edge velocity magnitude was measured by pitot-static probes mounted on the suction and pressure sides at three outer locations of the instrumented blade. As illustrated in figure 2*b*, the TE rakes had five pitot-static probes on the suction side and four on the pressure side, with

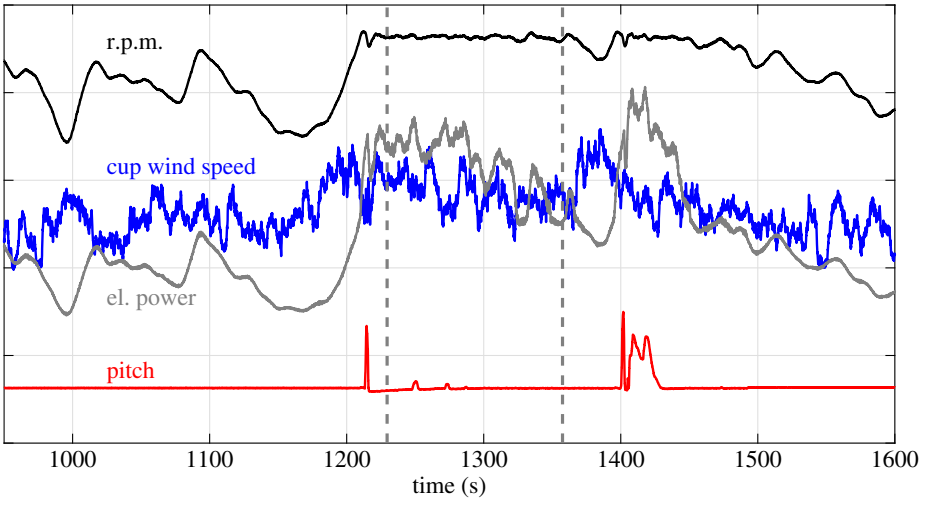

Figure 3. Time variations in blade pitch, electrical power, rotor r.p.m. and hub-height wind speed at the met. tower measured by a cup anemometer. The primary period of analysis (128 s) is the time period between the vertical dashed lines. The vertical axis scale is suppressed for proprietary reasons. (Online version in colour.)

the intention of capturing the boundary layer near the trailing edge (figure 2*b*). The suction-side probes had OD of 1.6 mm and ID of 0.46 mm, while the pressure-side probes had 1.07 mm OD and 0.406 mm ID pitot ports. The static ports of all probes on one side of the blade were collected in a manifold, averaging the static pressure readings into one each. These manifolds of ≈ 3 mm width and 8 mm length held the probes at the same time. The distance between the blade suction surface and the innermost TE rake probe was $h_s = 10$, 9 and 6 mm for the inboard, midboard and outboard rakes, respectively. These distances of the innermost probes from the pressure side were $h_p = 3$, 2.5 and 2 mm, respectively. The distance between the other probes on the suction side were $H_s = 10.5$, 9.5 and 6.5 mm for the inboard, midboard and outboard rakes, and the corresponding distances were $H_p = 4$, 3 and 2.5 mm for the probes on the pressure side of the blade. All probe tips were located 2.54 cm (l) upwind of the TE (along the surface). In §5c, the response of the trailing-edge boundary layer flow to atmospheric turbulence sensed by the LE probes is analysed using the TE rake data.

It should be noted that velocity magnitude is determined with pitot-static probes in the classical way using the steady form of the Bernoulli equation. As we apply the velocity data to draw conclusions about non-steady response, there may be justifiable concern with the neglect of the non-steady term in the classical pitot-static probe formula for velocity magnitude. Back-of-the-envelope estimates suggest that this concern is particularly relevant at response frequency well above the blade rotation frequency. (The neglect of the viscous force between the total and static pressure ports is quite justifiable.)

(c) Choice of the period for analysis

A 128 s time period was chosen for a detailed study of the field experiment and for comparison to an actuator line method (ALM) study and a planned blade boundary layer resolved computational fluid dynamics (CFD) study. Because the numerical simulations currently require fixed pitch and yaw and constant r.p.m., and because the focus is on understanding the interaction of the wind turbine with a moderately convective ABL, the field campaign dataset was explored for periods approximately satisfying these criteria. The variations in pitch, yaw, low-speed shaft r.p.m. and hub-height wind speed during this 128 s period are shown in figure 3, which is a subset of a 4136 s long period for which the met. tower and wind turbine data were collected

continuously (the values on the vertical axis could not be included for proprietary reasons). During this period, the mean wind speed measured by the cup anemometer on the met. tower near the hub height was 9.27 m s^{-1} (with a standard deviation of 0.93 m s^{-1}) and the wind turbine was operating at the higher end of region 2 in the power curve. The mean direction of the wind w.r.t. the met. tower to wind turbine direction (represented by x in figure 1) was 4.4° (with a standard deviation of 5.6°) for this period, implying that most of the ABL eddies observed by the met. tower probably passed through the wind turbine rotor.

3. The atmospheric boundary layer and its numerical generation using large-eddy simulation

The local and global structure of the daytime ABL is a strong function of the relative contribution of shear and buoyancy to the production of turbulence velocity fluctuations [1,13]. The presence of solar heating of the ground in the daytime creates strong atmospheric thermals. In the absence of wind, the daytime ABL will evolve to a fully convective state with vertical turbulence fluctuations generated by buoyancy production. However, wind turbines operate only in the presence of substantial wind, so that the daytime ABL relevant to wind turbine function over land in the USA and Europe is 'moderately convective'. As described in [1], in the MCBL buoyancy generates regions of concentrated positive and negative vertical velocity fluctuations ('updraughts' and 'downdraughts') that cause substantial mixing between the upper and lower ABL. The updraughts are strongly correlated with horizontally elongated 'low-speed streaks', ubiquitous coherent structures generated by the interaction between turbulence and strong mean shear rate near the ground. By contrast, in the nighttime ABL, heat flux is into the ground and shear dominates, as turbulence is continually suppressed by stable stratification. In the daytime MCBL, the transverse coherence length of both the low-speed streaks and the thermal updraughts in the atmospheric surface layer is of the order of the blade length and rotor diameter [16]. In this study, we focus on the influence of these rotor-scale flow structures on the blade loadings as they sweep through the rotor disc with the mean wind and generate highly non-steady loadings on the turbine blades, leading to premature fatigue failures of blades and bearings on the drivetrain.

The ABL conditions during the field experiment are quantified using the data from the met. tower and radiosonde data from a location 25 km from the site of the experiment. An ABL flow field which is close to the one quantified using the met. tower data is generated numerically using LES, for use as inflow condition for the subsequent numerical studies.

(a) Quantification of the atmospheric boundary layer stability state during the field test

It is known that the structure of ABL turbulence is a strong function of the global ABL stability state given by the ratio z_i/L [1,13,14], where z_i is the inversion layer height and L is the Obukhov length scale, an order-of-magnitude estimate of the height where buoyancy production of turbulence begins to dominate over shear production, which is dominant near the surface where shear is largest. The Obukhov length scale is given by

$$L = -\frac{{u_*}^3}{\kappa(g/\theta_0)Q_0}, \tag{3.1}$$

where u_* is the friction velocity, θ_0 is the reference potential temperature for the dry background state (roughly the mean temperature at the ground), κ is the von Karman constant, g is acceleration due to gravity and Q_0 is the mean surface temperature flux. A previous LES study [14] also suggests that, apart from z_i/L, the boundary layer depth z_i too has an influence on the near-surface ABL turbulent structures; hence care has been taken to ensure that the z_i during the data collection from the LES study is close to the corresponding value during the field test.

From the sonic anemometer on the met. tower (approximately the same distance from the ground as the wind turbine hub), the instantaneous and time-averaged (for the 4136 s period) momentum and temperature fluxes are calculated. It is known that for a stationary MCBL the variation of the mean fluxes from the surface to approximately the capping inversion height is nearly linear [13] (from Q_0 and ${u_*}^2$ at the surface to near zero at the capping inversion). Therefore, the mean fluxes estimated from the sonic measurements are linearly extrapolated to the surface to estimate Q_0 and u_*. These are estimated to be $0.14\,\mathrm{mK\,s^{-1}}$ and $0.77\,\mathrm{m\,s^{-1}}$, respectively. To evaluate uncertainty, we re-calculated surface fluxes assuming ±20% variation in boundary layer height. Variability in the estimates of u_* and Q_0 were found to be within 1% and 2% of the estimated values, respectively. The mean surface temperature (θ_0) during the experiment was approximately 293 K. The vertical potential temperature profile from radiosonde data (from a nearby airport) indicates z_i to be approximately 1800 m. Using these estimates of Q_0, u_* and θ_0, the Obukhov length L is calculated to be approximately −234 m, leading to a z_i/L estimate of −7.7. This is a typical value for an MCBL [1]. In the next section, the LES methodology to generate a similar ABL for use as inflow condition to the wind turbine for the numerical study will be explained.

(b) Generation of the numerical atmospheric boundary layer approximating the field test

For the ALM study, the ABL inflow facing the wind turbine in the computational domain is required to be approximately similar to the one facing the wind turbine during the field experiment. To generate such an ABL, we apply the massively parallel pseudo-spectral LES code of Sullivan *et al.* [17]. LES is a technique which resolves the large integral-scale eddies responsible for turbulent momentum and temperature fluxes and models the effects of the smaller-scale unresolved eddies on the resolved scales. In terms of ability to resolve the broad spectrum of turbulent length and time scales, LES lies somewhere between Reynolds-averaged Navier–Stokes (RANS) on one extreme (which resolves only scales commensurate with the ensemble mean) and direct numerical simulation (DNS) on the other (which resolves turbulence down to the viscous scales). For studying very high-Reynolds-number ABL flows, whereas RANS predictions lack the ability to resolve the dynamics of all the relevant scales, DNS can be prohibitively expensive. In LES a spatial filter is applied so that turbulence length scales larger than the filter size are resolved while the diffusive effects of turbulent motions at scales below the filter size are modelled using a subfilter-scale model. The filtered Navier–Stokes and energy equations are solved in the LES methodology to predict the evolution of the large eddies.

(i) Overview of the large-eddy simulation methodology

The instantaneous velocity $\mathbf{u}(\mathbf{x}, t)$ and temperature $\theta(\mathbf{x}, t)$ fields are decomposed into filtered components $\tilde{\mathbf{u}}(\mathbf{x}, t)$ and $\tilde{\theta}(\mathbf{x}, t)$, and subfilter components $\mathbf{u'}(\mathbf{x}, t)$ and $\theta'(\mathbf{x}, t)$, respectively. Transport equations for these filtered quantities are solved along with a Poisson equation for pressure. A one-equation LES subfilter-scale stress model [18] is used to model the unclosed terms in the equations for the filtered quantities [17]. The filtered momentum equation is expressed as

$$\frac{\partial \tilde{\mathbf{u}}}{\partial t} + \tilde{\mathbf{u}} \cdot \nabla \tilde{\mathbf{u}} = -\mathbf{f} \times (\tilde{\mathbf{u}} - \mathbf{u}_\mathrm{g}) - \frac{1}{\rho_0} \nabla p^* + \frac{\mathbf{g}}{\theta_0}(\tilde{\theta} - \theta_0) - \nabla \cdot \boldsymbol{\tau}_\mathbf{u} + \mathbf{F}, \tag{3.2}$$

where $\mathbf{f}$ is the Coriolis parameter, $\mathbf{u}_\mathrm{g}$ is the geostrophic wind vector and θ_0 is the reference potential temperature. $\boldsymbol{\tau}_\mathbf{u}$ represents the anisotropic part of the subfilter stress tensor $\mathbf{r} = \widetilde{u_i u_j} - \tilde{u}_i \tilde{u}_j$). The isotropic part of $\mathbf{r}$ is absorbed inside the filtered pressure term, and the resulting pressure is referred to as the effective pressure (p^*). $\boldsymbol{\tau}_\mathbf{u}$ is modelled using the eddy viscosity hypothesis, where it is related to the filtered rate-of-strain tensor ($\tilde{\mathbf{s}}$) through the subfilter-scale eddy viscosity parameter $\nu_{tu,\mathrm{SFS}}$,

$$\boldsymbol{\tau}_\mathbf{u} = -2\nu_{tu,\mathrm{SFS}} \tilde{\mathbf{s}}. \tag{3.3}$$

Modelling of $\nu_{tu,\mathrm{SFS}}$ requires prescribing a velocity scale and a length scale. The velocity scale is obtained from the subfilter-scale turbulent kinetic energy (e), which in turn is obtained from its transport equation modelled as

$$\frac{\partial e}{\partial t} + \tilde{\mathbf{u}} \cdot \nabla e = \nabla \cdot (2\nu_{tu,\mathrm{SFS}} \nabla e) - \boldsymbol{\tau}_{\mathbf{u}} \tilde{\mathbf{s}} + \frac{g}{\theta_0} \boldsymbol{\tau}_{\boldsymbol{\theta}} - c_\epsilon \frac{e^{3/2}}{l}, \tag{3.4}$$

where the terms on the r.h.s. represent the diffusion, shear production, buoyant production and dissipation of e; $\nu_{tu,\mathrm{SFS}}$ is related to e as

$$\nu_{tu,\mathrm{SFS}} = c_k l \sqrt{e}. \tag{3.5}$$

In the present formulation, the length scale l is taken to be proportional to the characteristic grid size (Δ) for unstable stratification. In the stably stratified capping inversion, $l = 0.76e^{1/2}/[(g/\theta_0)(\partial\theta/\partial z)]$.

F in equation (3.2) is a body-force term in context with the actuator line model for wind turbine blades discussed in §4. This term was not active while generating the numerical ABL flow field. Manipulating equation (3.2) along with the continuity equation for the filtered velocity field leads to the Poisson equation for the effective pressure,

$$\nabla^2 p^* = b, \tag{3.6}$$

where the term on the r.h.s. b results from the above-mentioned manipulation. The transport equation for the filtered potential temperature field $\tilde{\theta}(\mathbf{x}, t)$ is formulated as

$$\frac{\partial \tilde{\theta}}{\partial t} + \tilde{\mathbf{u}} \cdot \nabla \tilde{\theta} = -\nabla \cdot \boldsymbol{\tau}_{\boldsymbol{\theta}}, \tag{3.7}$$

where $\boldsymbol{\tau}_{\boldsymbol{\theta}}$ represents the subfilter-scale potential temperature flux $(\widetilde{u_i\theta} - \tilde{u}_i\tilde{\theta})$. As the characteristic Reynolds number for ABL flows is usually very high and the ABL is a rough-surface boundary layer, a viscous sublayer does not exist and is replaced by roughness elements characterized in the surface stress boundary condition [18] by a single homogeneous roughness scale $z_0 \ll z_i$. Hence, the molecular diffusion terms are neglected in the governing equations. The sub-filter scale temperature flux is also modelled using the eddy viscosity hypothesis,

$$\tau_\theta = -\nu_{t\theta,\mathrm{SFS}} \nabla \tilde{\theta}, \tag{3.8}$$

where $\nu_{t\theta,\mathrm{SFS}} = (1 + 2l/\Delta)\nu_{tu,\mathrm{SFS}}$.

The code solves the governing equations using the pseudo-spectral method in the horizontal planes and second-order finite differencing (on a staggered grid) in the vertical planes [17,18].

(ii) Mesh requirements and numerical details

The horizontal size of the domain is taken as 5×5 km ($L_x \times L_y$) and the height of the domain is taken as 2.7 km (L_z). Because the inversion layer height during the chosen period of analysis was approximately 1.8 km, L_z is chosen to be $1.5z_i = 2.7$ km to allow the unconstrained evolution of the numerical ABL top. The choice of L_x and L_y is based on the requirement to capture several convective rolls which play a critical role in transferring momentum and temperature flux across the ABL and have horizontal length scales $\mathcal{O}(z_i)$.

Initial simulations were carried out using a $128 \times 128 \times 128$ mesh, where an iterative approach was adopted to arrive at an approximate numerical ABL which closely matches the ABL conditions during the field test. Attempts were made to arrive at an ABL state with similar hub-height wind speed, ABL stability state z_i/L and ABL inversion layer height z_i. The geostrophic wind speed, strength of capping inversion and surface roughness height (which were not readily available) were adjusted iteratively in the LES code to get close to the correct ABL conditions.

The final simulation is carried out using a $768 \times 768 \times 256$ mesh to properly resolve the primary relevant length and time scales which influence the magnitude and time variation

in blade aerodynamic loadings. To remove aliasing errors, the two-thirds-rule is used in the horizontal directions. Time advancement is done using a third-order Runge–Kutta scheme, using a fixed Courant–Friedrichs–Lewy (CFL) number of 0.5.

A three-layer potential temperature profile is prescribed as the initial condition. The initial capping inversion height is defined at 1300 m. The potential temperature is constant from the surface to 1250 m, followed by a linear increase of 15 K over the next 100 m. Beyond that we specify a gentle potential temperature gradient (0.003 K m^{-1}) to the top of the computational domain.

(c) Spatial and temporal location of the domain for the actuator line method study in the atmospheric boundary layer field

Data were collected from the LES study for a duration of 2587 s, when the horizontally averaged hub-height wind speed, the stability state z_i/L and the inversion height z_i were close to the corresponding quantities from the field test. To do a quantitative comparison of the LES and the field test datasets, the met. tower data are also analysed for 2587 s, located around the 128 s long time period for detailed study. The integral time scale associated with the daytime ABL eddies is $\mathcal{O}$(1 min), so a period of 2587 s is sufficient to accommodate the passage of multiple eddies through the rotor plane.

From the LES dataset, which contains the velocity vector and temperature data at $768 \times 768 \times 256$ discrete points, 23 points each at three streamwise locations ($x/L_x = 0.05, 0.5$ and 0.95) were extracted near the sonic height for comparison with the field sonic data. The 23 points were equally spaced in the spanwise direction. The motivation was to find the location in the LES domain which shows good correlation with the sonic data for the 2587 s period, and particularly for the 128 s period chosen for the detailed analysis and comparison with numerical studies.

Integral time scales corresponding to the ABL eddies based on the streamwise and vertical components of velocity ($\tau_{l,uu}$ and $\tau_{l,ww}$, respectively) were estimated for the sonic and the LES datasets, from the corresponding autocorrelation functions, which were integrated to the first zero crossing to estimate $\tau_{l,uu}$ and $\tau_{l,ww}$. For the sonic data, these values were calculated to be approximately 48 s and 18 s, respectively. Estimates from 69 points in the LES domain were compared with those extracted from the sonic data. From these 69 points, eight points were chosen where the difference between the integral time scale estimates between the LES and the sonic data were within 20%. The time series of the velocity components at these eight locations were studied carefully to identify the spatial and temporal locations where good correspondence between the sonic and the LES data is observed. This process led us to choose a 128 s period at $x = 273$ m, $y = 1400$ m in the LES domain, where maximum correspondence with the field data was observed. Data over the vertical plane at this location were extracted to provide time-varying inflow to the computational domain for the subsequent numerical studies as per [19].

Figure 4 shows the comparison of the time-averaged velocity magnitude obtained from the cup anemometers with the corresponding quantities extracted from the LES data at the chosen location in the LES domain. The legends LES 1, LES 2 and LES 3 refer to the wind profiles from the LES study using different extents of spatio-temporal averaging (more details are provided in the caption of the figure). Good comparison can be observed between the field test and LES wind profiles. Figure 5 shows the ABL inflow $0.5D$ (where D is the rotor diameter) in front of the rotor plane (from the ALM study using ABL inflow), indicating strong spatial variability with length scales comparable to the rotor diameter. In addition to vertical wind shear, a significant variation in wind speed exists within the rotor plane. Strong temporal variability exists in transverse gradients as well as local fluctuations, with transverse scales $\sim \mathcal{O}$(blade radius), possibly contributing significantly to asymmetry in blade loadings. Such detailed information about the spatial variability of the ABL flow is not available from the field data obtained from single sensors on a single met. tower.

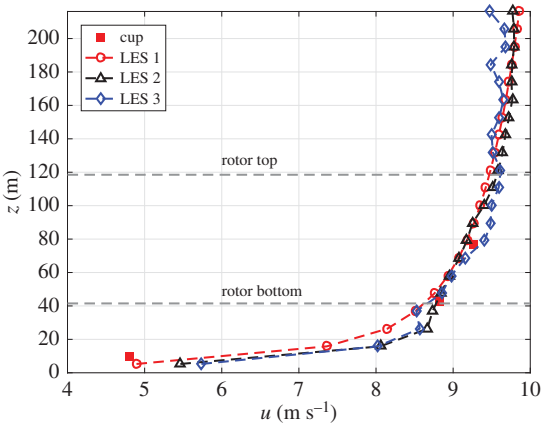

Figure 4. Comparison of the wind speed profile obtained from the met. tower and the LES study. Legends: cup: 128 s time-averaged cup anemometer data from the met. tower. LES 1: spatially averaged over the 5 × 5 km horizontal planes, and time-averaged over approximately 10 000 s around the 128 s period of analysis. LES 2: spatially averaged over the spanwise direction at the vertical plane chosen for prescribing the inflow to the ALM domain, and time-averaged over 128 s. LES 3: No spatial averaging, data collected at the vertical plane chosen for prescribing the inflow to the ALM domain, at the spanwise location at which the met. tower would have been present; time-averaged over 128 s. (Online version in colour.)

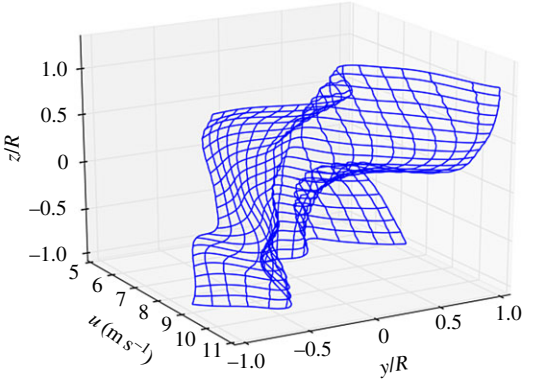

Figure 5. Instantaneous ABL velocity component perpendicular to the rotor plane (u), calculated 0.5 rotor diameter in front of the rotor plane (obtained from the ALM simulation using ABL inflow). R is the blade radius, and $(y, z) = (0, 0)$ is along the axis of rotation of the rotor. z is in the direction perpendicular to the Earth's surface, and y is perpendicular to z and the rotor axis. Spatial variability with length scales comparable to R can be observed. (Online version in colour.)

4. The actuator line method formulation for the GE 1.5 MW rotor within the atmospheric boundary layer

The ALM is a lower-order method (compared with blade boundary-layer-resolved CFD study) to model wind turbine blade loads by a modelled spanwise distribution of body forces whose strengths are functions of sectional inflow conditions. Although this method is not capable of providing blade-resolved flow field data because it models net local effects of blade loadings on the neighbouring flow field while using local flow angles and lift/drag polars obtained from wind tunnel experiments to model sectional loads, it provides reasonable estimates of wind turbine blade loadings with reasonable computational cost (compared to blade boundary-layer-resolved simulation). For this study, the ALM solver within the OpenFOAM [20] framework developed

by Jha *et al.* [15] is used to calculate the blade aerodynamic response and wind turbine loadings and is compared and contrasted with the 128 s long experimental data. The blade pitch and rotor r.p.m. are kept equal to those during the experimental analysis period. The ALM simulation is further run for a longer time period to capture the influence of a broader range of eddy types on blade loadings and to generate ensemble-averaged statistics.

In the incompressible Navier–Stokes equation (equation (3.2)), the term **F** on the r.h.s. represents the body-force term for the actuator line formulation. The discrete actuator point loads are projected to form the volumetric body-force term using the relationship

$$\mathbf{F}(x,y,z,t) = -\sum_{N}\sum_{m} \mathbf{f}_{N,m}(x_{N,m},y_{N,m},z_{N,m},t)\eta_{N,m}, \tag{4.1}$$

where

$$\eta_{N,m} = \frac{1}{\epsilon_m^3 \pi^{3/2}} \exp\left[-\left(\frac{|\mathbf{r}_m|}{\epsilon_m}\right)^2\right]. \tag{4.2}$$

Here **f** is the load on each discrete actuator point, N represents the blade index and m represents the actuator point index, $|\mathbf{r}_m|$ is the distance from grid cell centre to the actuator point and ϵ_m is the radius of the body-force projection function η. **f** at each actuator location is calculated from the local velocity vector and aerofoil lift/drag polars.

While in conventional ALM [21,22], the projection radius ϵ_m is related to the local grid width, Jha *et al.* [15] developed a methodology where the projection radius varies along the blade span following an elliptic distribution. This $\epsilon_m/c_m^* = \text{constant}$ methodology (where c_m^* is the equivalent elliptic planform for the blade at the location of the mth actuator point) was shown to perform better in predicting the loads near the tip compared with the conventional approach. Jha *et al.* [15] provide guidelines to increase prediction accuracy through the choice of ALM parameters, including ϵ_m, grid spacing along the actuator line (Δ_g) and the spacing between actuator points (Δ_b).

The computational domain is rectangular in shape, with dimensions of $800 \times 500 \times 220$ m. The mesh consists only of hexahedral elements, with refinement being done in the region near the rotor plane, where the grid size is taken as $1 \times 1 \times 1$ m (i.e. $\Delta_g = 1.0$ m conforming to the recommendation that Δ_g/R should be between $\frac{1}{64}$ and $\frac{1}{32}$). The model uses spanwise-varying Gaussian width $\epsilon_m/c_m^* = 1.6$. Each blade is represented using 25 uniformly distributed actuator points, leading to the ratio of actuator spacing to grid length scale (Δ_b/Δ_g) of approximately 1.5. The initial conditions for the ALM study were obtained from the ABL field at the corresponding time from the LES simulation. Also, the ABL field corresponding to the ALM inflow plane was provided as the Dirichlet boundary condition (as a function of time) for the velocity components, temperature and subfilter-scale turbulent kinetic energy.

The time step is chosen such that the blade tips do not traverse more than one grid cell per time step. Within an LES formulation, a one-equation eddy viscosity model [18] is used to model the subfilter-scale stress tensor. The simulation is initiated 130 s before the start of the period for comparison with the field test, to ensure that the data collected are free from the influence of the initial transients. The data are collected for a total of 800 s.

5. Non-steady wind turbine responses to atmospheric boundary layer inflow

In §5a, c and d, the response of the GE 1.5 MW wind turbine to daytime atmospheric turbulence using time-resolved localized blade aerodynamic data together with SCADA data from the GE field campaign is analysed. As described in §3a and b, the stability state of the field ABL during the data collection period is estimated from meteorological data and an equivalent ABL is generated with high-resolution LES. An actuator-line-modelled GE wind turbine is placed within the numerical ABL field at a space-time location that closely represents the period of analysis in field data. Comparisons between the numerical and field data are described in §5b.

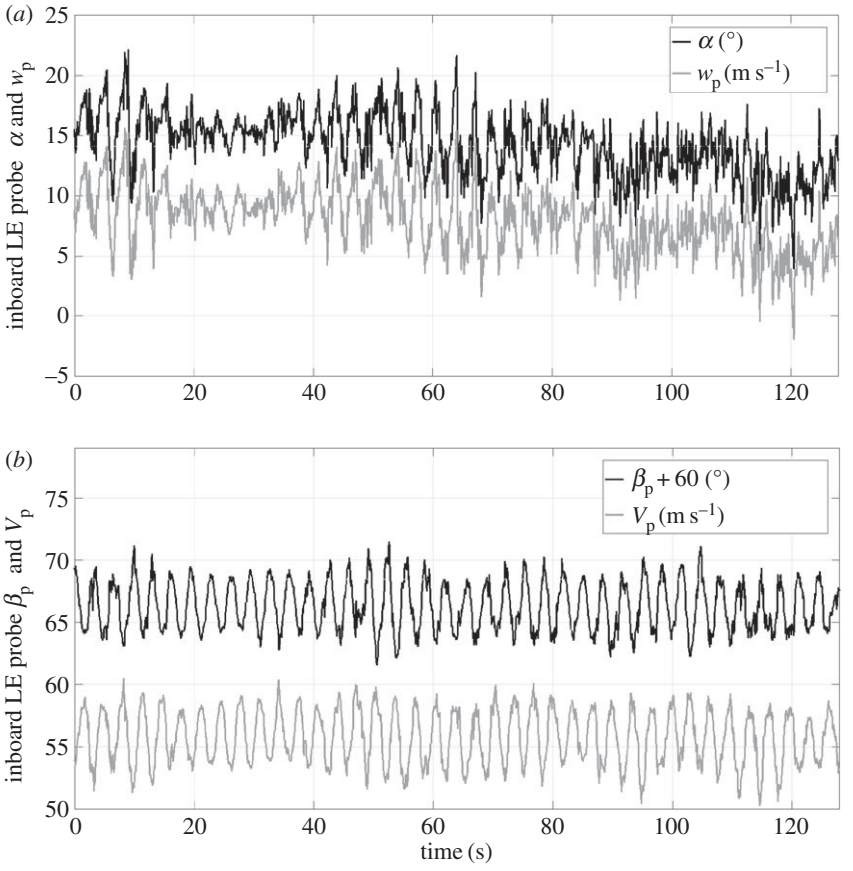

Figure 6. Comparison of the inboard leading-edge probe quantities from the experiment. (*a*) Inflow angle α and velocity component w_p. (*b*) Inflow angle β_p (shifted by 60°) and velocity magnitude V_p.

(a) Blade inflow response analysed with the GE field data

As described in §2b and illustrated in figure 2, one of the wind turbine blades in the GE field campaign was instrumented with five-hole pitot probes off the leading edge at three locations along the outer 30% of the blade. These data are available at a sampling rate of 16 Hz. With these probes the non-steady local velocity vector $\mathbf{V}_p(t)$ was measured relative to the rotating blade sections in response to the passage of daytime atmospheric turbulence eddies. In figure 6*a* we plot, over the 128 s period of analysis (figure 3), the time-resolved flow angle $\alpha = \alpha_p + 6^\circ$ of $\mathbf{V}_p$ relative to the local aerofoil sectional chord (figure 2*a*) together with the velocity component w_p perpendicular to the local blade planform area (roughly in the direction of the x component of the wind velocity vector illustrated in figure 1). Although α is not equivalent to angle of attack (and no attempt is made to modify α for induced velocity), one might interpret the non-steady response in sectional lift and drag coefficients relative to time changes in the local flow angle α as a rough qualitative surrogate to the non-steady response in sectional force coefficients from time changes in angle of attack. In figure 6*b*, we plot the time changes in spanwise angle β_p, together with time variations in the magnitude of the relative velocity, $V_p = |\mathbf{V}_p|$.

In figure 6*b*, the most prominent time scale is the blade rotation time (3.3 s), the once-per-revolution (1P) variation that results from the interaction between the rotating blade and the velocity variations due to the internally heterogeneous structure of turbulence eddies passing through the rotor plane. This variation includes the effect of long-time average mean shear variation between the upper and lower margins of the rotor disc, estimated in figure 4 to

be $\approx 0.8\,\mathrm{m\,s^{-1}}$, or $\approx 13\%$ of the average $6.3\,\mathrm{m\,s^{-1}}$ peak-to-peak variation in V_p. However, there are two other time scales apparent in figure 6*b*: a longer time scale indicated by the modulations in the envelope surrounding the peak-to-peak variations, and shorter-time-scale fluctuations that ride on top of the 1P variations. As will be discussed, the longer-time variations are ≈ 25–$50\,\mathrm{s}$ long, and are associated with the passage of dominant energetic turbulence atmospheric eddies through the rotor plane at the convection time scale, while the short-time-scale fluctuations are $\approx 1\,\mathrm{s}$ or less associated with blade response to internal eddy structure.

The time variations in the out-of-aerofoil-plane relative flow angle β_p are qualitatively similar to the time variations in V_p, where V_p is dominated by the chordwise velocity component at the probe location, u_p (figure 2). In both cases the 1P variation is clearly dominant. However, the time variations in α and w_p are also qualitatively similar, but fundamentally different from V_p and β_p in two important ways. Firstly, whereas the 1P variation is dominant throughout the time series of β_p and V_p (and also both u_p and v_p, which are not shown), the 1P variations are dominant only intermittently in the fluctuations of α and w_p. For example, although the 1P variations exist throughout the signals in figure 6*a*, they are much less apparent during the periods 20–40 s and 90–130 s. Interestingly, periods where the 1P variations are not apparent are also periods where the peak-to-peak excursions in the signal are suppressed, suggesting that these periods may be associated with turbulence fluctuations that are not directly associated with the periodic 1P response. Further, in the α and w_p time variations, the high-frequency (less than 1 s) oscillations are qualitatively more prominent than in β_p and V_p fluctuations. Nevertheless, the longer-time variations are readily apparent and qualitatively line up with the longer-time fluctuations in β_p and V_p.

Clearly, there exist at least two related but different characteristics in the temporal response of velocity vectors upwind and local to the rotating blades: the in-aerofoil-plane flow angle α and the velocity vector component perpendicular to the local blade planform w_p have very similar time variations as per figure 6*a*. However, the temporal characteristics of α and w_p are different in significant detail from the time variations in the spanwise flow angle β_p and in velocity magnitude V_p, as well as in velocity components in the chordwise and spanwise directions u_p and v_p (not shown).

Similarly, these important distinctions are reflected in the frequency spectra of the same signals shown by the black curves in figure 7 (the grey spectra from the ALM dataset will be discussed in the next section). Immediately apparent in these spectra is the existence of three dominant characteristic time scales. (i) The 1P component of the signals in figure 6 is apparent as a spectral peak in figure 7 at $\approx 0.3\,\mathrm{Hz}$. The 1P time scale of 3.3 s results from the periodic passage of the blade through the heterogeneous turbulent velocity field within atmospheric eddies. The first harmonic of this 1P frequency (at 0.6 Hz) is also apparent in figure 7. (ii) The spectrum rises at lower frequencies to reach a peak in the range 0.02–0.04 Hz, corresponding to a time scale ≈ 25–$50\,\mathrm{s}$. This time scale appears in the envelopes of the time variations shown in figure 6, where about four eddy passages are apparent in the 128 s sample, consistent with the 0.02–0.04 Hz in the plateau in the spectra of figure 7. (iii) A roughly power-law decay is observed at the highest frequencies in figure 7. This power-law decay peaks at energies commensurate with the lower-frequency portions of the spectra, at frequencies ≈ 1–$2\,\mathrm{Hz}$, corresponding to time scales ≈ 0.5–$1\,\mathrm{s}$. The spectra also display an interesting minimum at frequencies a factor of two to three lower than the 1P frequency peak, in the range 0.1–0.2 Hz (≈ 5–$10\,\mathrm{s}$). As discussed at the end of this section, this is associated with the rotating frame of reference in which the blade data were collected.

The distinctions drawn between the characteristics of the fluctuating variables β_p and V_p versus α and w_p in figure 6 are reflected by differences in spectral content in figure 7. We note, specifically, that the dominant 1P periodic variation in β_p and V_p is reflected by a very sharp peak in the β_p and V_p spectra while, by contrast, the spectral content surrounding the 1P peaks in α and w_p is much broader and less well defined, similar qualitatively to the time variations in α and w_p in figure 6, which display periods in which the 1P variation is only minimally evident, in contrast with β_p and V_p, which clearly display a 1P periodicity at all times. Furthermore,

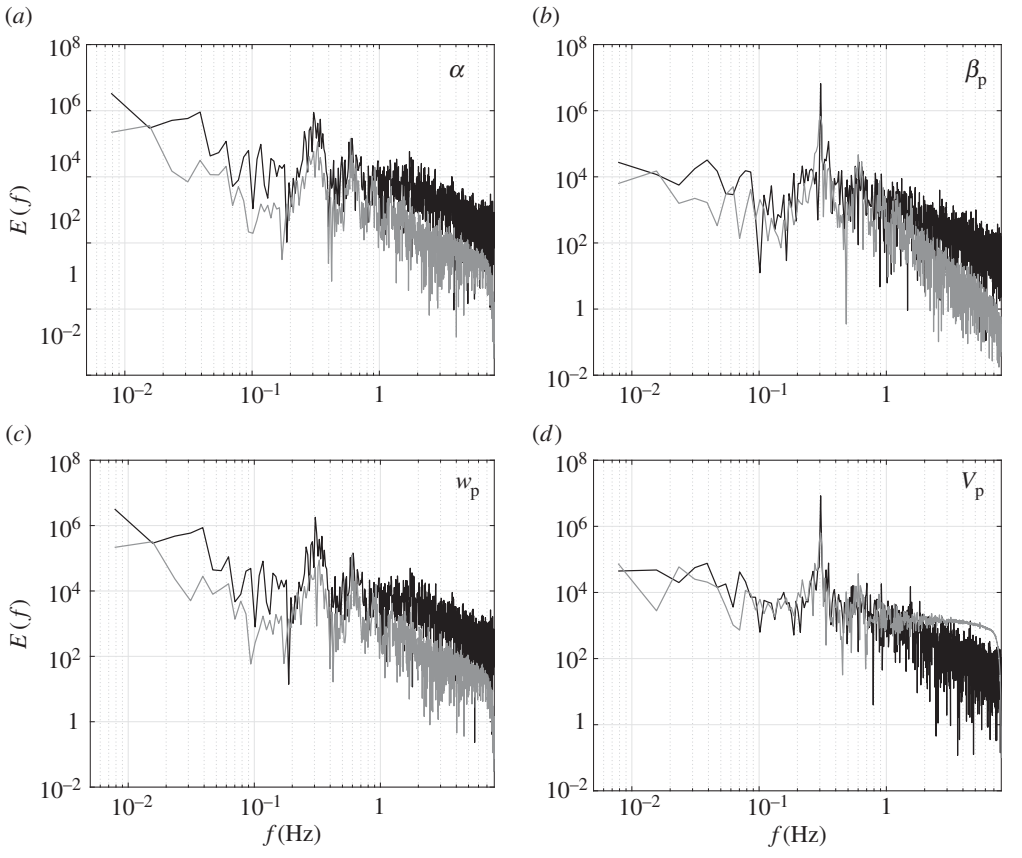

Figure 7. Spectra of the inboard leading-edge quantities from the field experiment (black) and the ALM study (grey) for the 128 s period. (*a*) Inflow angle α. (*b*) Inflow angle β_p. (*c*) Velocity component w_p. (*d*) Velocity magnitude V_p (figure 2*a*).

the apparently higher variance in the non-1P parts of the α and w_p signals compared with the non-1P variations in β_p and V_p is reflected, in their corresponding spectra, by significantly higher levels of spectral energy near 1 Hz in the α and w_p spectra compared with the β_p and V_p spectra.

What cannot be ascertained from the spectra is the observation, in figure 6, that the temporal variations of local velocity flow angle α in the local plane of the blade section have an intermittent character in time that closely matches that of the velocity component w_p and that these temporal variations are very different in fundamental ways from other local fluctuations associated with the velocity vector V_p. Why is that? To address this question, we refer to figures 1 and 2*a* and note that the local velocity component w_p relative to the rotating blade illustrated in figure 2*a* is approximately in the same direction as the wind velocity component u along the x axis illustrated in figure 1. That is, w_p is directly forced by the horizontal fluctuating velocity within the turbulence eddies passing through the rotor plane. This is not the case for any other velocity component of $\mathbf{V}_p$.

We conclude that w_p is directly responding to atmospheric turbulence eddy passage through the fluctuations in horizontal wind velocity, in contrast with other components of $\mathbf{V}_p$, which are only indirectly influenced by turbulence fluctuations in the atmospheric winds. Importantly, the strong correspondences between the temporal variations in α and w_p in figure 6*a*, and between their spectra in figure 7*a*,*c* (especially in contrast with β_p and V_p in figures 6*b* and 7*b*,*d*), suggest that the in-aerofoil-plane flow angle α is directly forced by atmospheric turbulence, while the out-of-aerofoil-plane (spanwise) flow angle is not. Given the likely strong correlation between the fluctuations in α and the fluctuations in sectional lift coefficients, these results indicate a

direct important forcing of blade loadings by atmospheric turbulence eddy passage. Furthermore, given that the length scale of the coherent energy-containing atmospheric eddies is of the order of the rotor diameter, this direct forcing of sectional blade loadings probably produces a coherent response over the entire blade, and therefore in the mechanical torque and power from the blade to the wind turbine low-speed shaft through the hub.

In §5d, we discuss this result in context with the measured electrical power at the generator on the wind turbine high-speed shaft side. We find that, whereas the high-frequency characteristics measured on a single blade do not persist through the drivetrain and generator, the low-frequency modulations associated with atmospheric eddy passage do persist and strongly modulate electrical power variations. As the advective eddy passage time scale is an order of magnitude longer than the blade rotation time scale, the longer-time-scale variations in blade loadings may be reasonably modelled as quasi-stationary.

The dip in the spectra between the frequencies corresponding to the large-eddy time scale and the 1P time scale is a direct consequence of the rotational sampling of the atmospheric turbulence by the probe(s) on the rotating blade. Connell [23] suggests that the spectrum obtained from a probe rotating through a turbulent field differs from that obtained with a stationary probe due to transfer of energy from mid to higher frequencies resulting in a dip at the mid frequencies, and the accumulation of energy at frequencies higher than the 1P frequency. The effect is strongest at higher tip-speed ratios, and larger ratios of the blade length and eddy integral length scale. A strong correlation exists between the signals from the leading-edge probes at the three spanwise locations in the GE dataset, implying that they experience the same ABL eddy structure, and the integral length scale of the ABL turbulence eddies is larger than the maximum spanwise separation between these probes (8 m).

(b) Comparison of field data and actuator line method predictions of blade inflow response

It is of particular interest to assess the ability of the actuator line methodology to capture the blade aerodynamic response to ABL turbulence. It is observed that the leading-edge aerodynamic response at the blade revolution time scale is also observed from the ALM dataset (figure 7, the grey spectra), where the spectra of α, β_p, w_p and V_p from these two datasets (available at the same sampling rate of 16 Hz) have been compared. It can be observed that the thrice-per-revolution (3P) peak is relatively more prominent in the ALM data compared with the field data. Also, the energy content of the signals around the 1P frequency peak is higher for the quantities obtained from the field experiment when compared with those from the ALM study. These differences can be possibly attributed to structural vibrations of the wind turbine (which contribute to blade and probe fluctuations) in the field experiment, which are not accounted for in the ALM study. Also, the relatively lower energy in the high-frequency region in the ALM dataset (compared with the leading-edge probe dataset from the field experiment) is likely due to lack to higher-frequency resolution in the precursor LES dataset, and this part of the spectrum is very much susceptible to numerical artefacts.

The higher harmonics (in both the experimental and ALM datasets) are not very prominent due to lack of samples in this 128 s period, which is confirmed by the observation that peaks at these frequencies become discernible in the spectra for the 800 s long ALM simulation. Such an observation cannot be made from the experimental data, as the r.p.m. changes continuously over any duration longer than the 128 s period, leading to non-unique 1P frequency and its harmonics.

Also, from the ALM data it can be observed that the peak at higher harmonics in leading-edge probe inflow angle α (figure 8), and hence the sectional loads, becomes stronger with increasing radial distance (being quite prominent in the blade outboard regions where mean as well as fluctuating bending moments are relatively high), indicating the strong non-homogeneity in the inflow of the order of the blade length scale. The higher harmonics in the blade aerodynamic response are mainly due to the blade outer sections sweeping through multiple such non-uniform regions in the inflow during a single revolution of the blade.

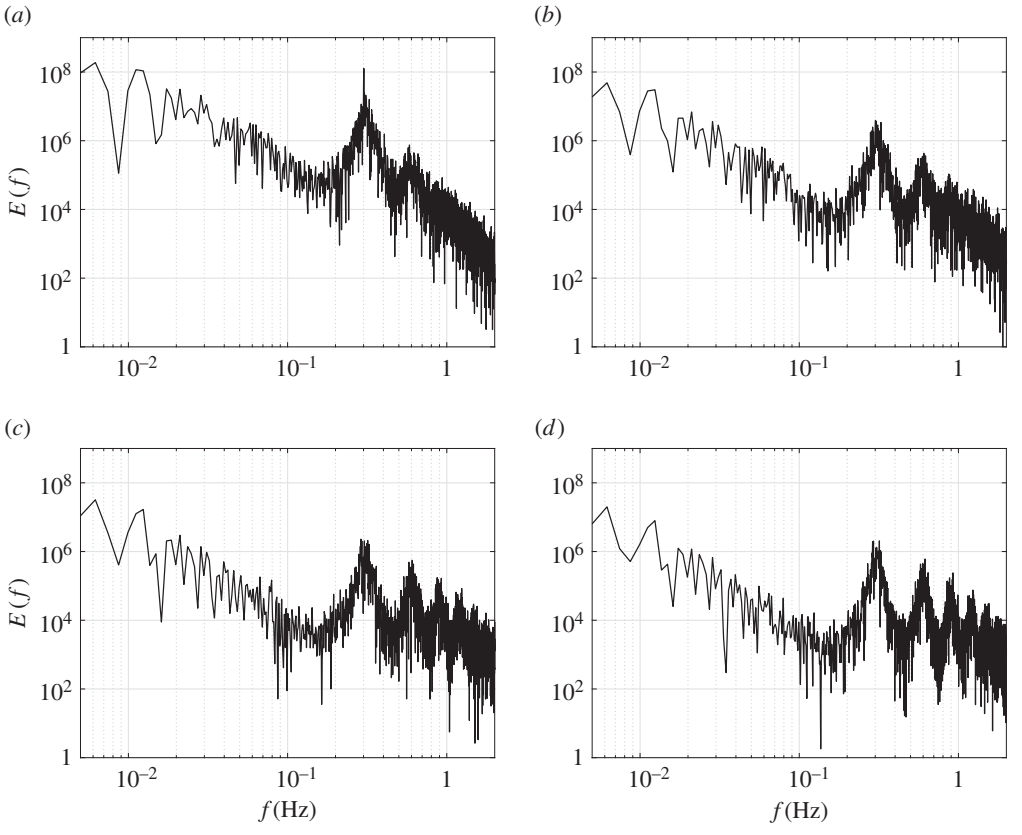

Figure 8. Comparison of the spectra of the leading-edge probe inflow angle α from the 800 s long ALM study at (*a*) 20%, (*b*) 40%, (*c*) 60% and (*d*) 80% blade radial locations.

(c) Response of the blade boundary layer analysed with the GE field data

The instrumented blade carried pitot-static rakes at three outer sections with the intention of capturing the boundary layer near the trailing edge. From §5a, it was observed that the blade leading-edge inflow angle α and the velocity component w_p are strongly modulated by atmospheric turbulence. It is of interest to understand how the blade boundary layer responds to ABL turbulence, as well as how it is correlated to the blade leading-edge inflow.

Figure 9 shows the time-averaged (128 s) TE rake velocity gradient profile obtained from the three rakes on the suction surface, indicating classical adverse pressure gradient boundary layer. Also observed is the decrease in the time-averaged trailing-edge boundary layer thickness from the inboard to the outboard rake locations. Figure 10*a* shows the time series of the velocity magnitude from the rake on the suction surface (at the inboard location, with the three measurements taken at distances of 10.0, 31.0 and 52.0 mm from the blade surface). It can be observed that, while strong 1P variations are observed throughout the 128 s period in the signal from the probe furthest from the blade surface, this periodic variation is relatively less prominent at the probe nearest to the blade surface. Similar to the observation from the leading-edge α and w_p, the velocity magnitude measured from the innermost probe shows an intermittent behaviour, and the temporal locations of the clearer 1P variation coincide approximately with those from the leading-edge α and w_p signals (figure 6*a*) indicating the influence of atmospheric turbulence (to which the surrogate angle of attack α responds strongly) on the boundary layer dynamics. On the contrary, the flow measured by the outermost probe is relatively less sensitive to the time variations in α and w_p, and rather well correlated with the inflow velocity magnitude V_p. This

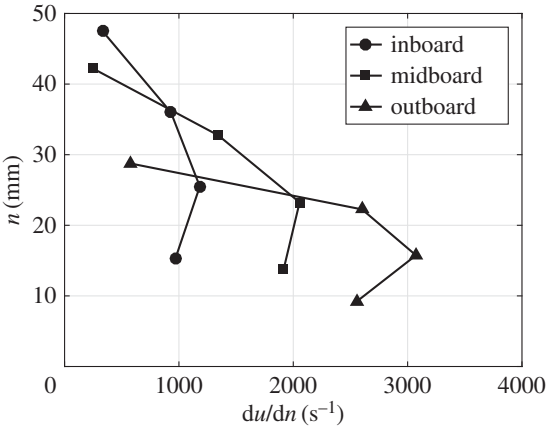

Figure 9. Time-averaged (128 s) TE rake velocity magnitude gradient profile (suction side) at the three spanwise locations. *n* is in the direction normal to the local blade surface.

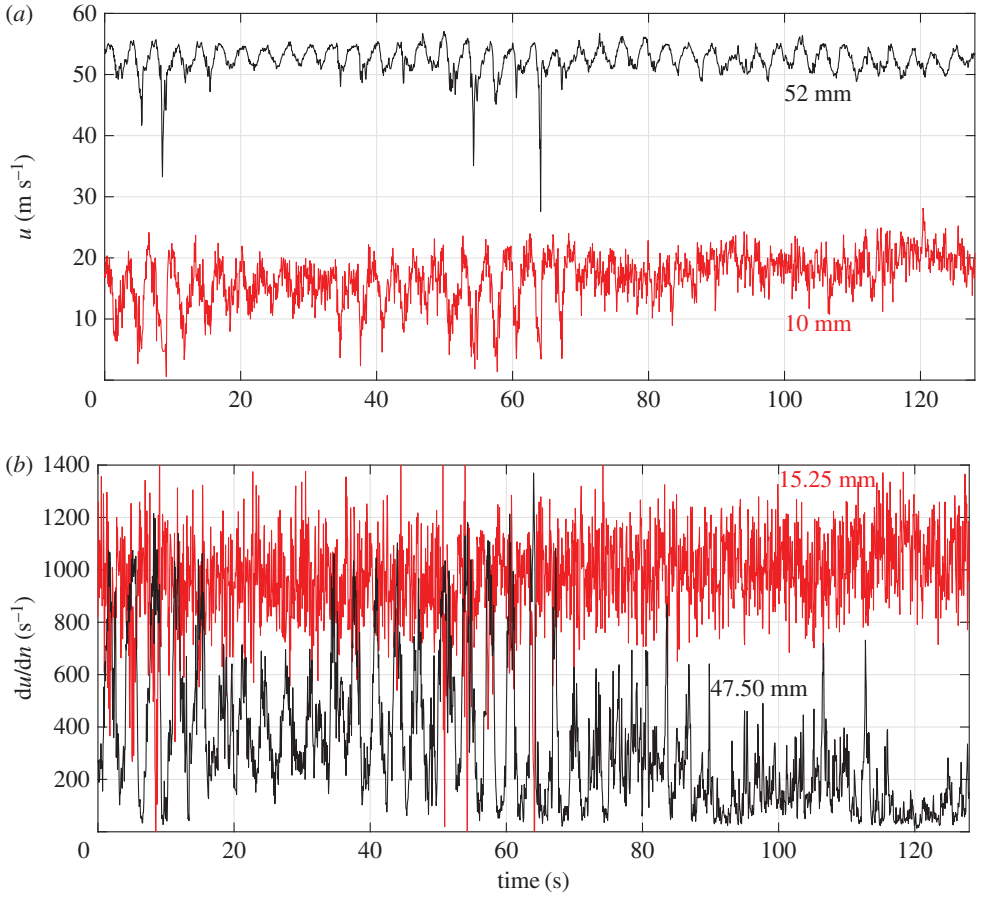

Figure 10. Time series of inboard TE rake (*a*) velocity magnitude, at distances of 10 mm and 52 mm from the suction surface, and (*b*) velocity magnitude gradient, at distances of 15.25 mm and 47.5 mm from the suction surface. (Online version in colour.)

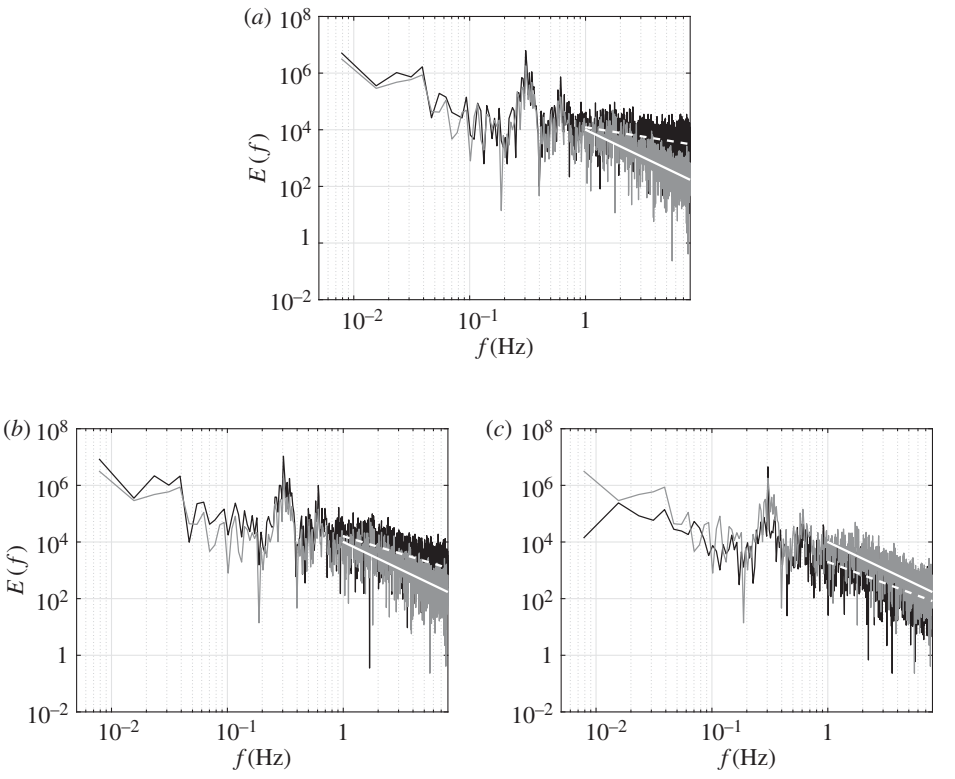

Figure 11. Comparison of the spectra of inboard LE probe w_p (grey) and velocity magnitude from inboard TE rake probe (black): (*a*) 10 mm from the suction surface, (*b*) 31 mm from the suction surface and (*c*) 52 mm from the suction surface. The solid and the dashed white lines represent the slopes of the high-frequency region, for the LE probe w_p and velocity magnitude from the TE rake probes, respectively.

can be attributed to the fact that the innermost probe, being well inside the boundary layer, is strongly modulated by the local angle of attack (for which α is a surrogate), which is in turn driven by the atmospheric horizontal fluctuations quantified by w_p, whereas the outermost probe, located in the nearly irrotational flow in the outer part or outside the boundary layer, primarily responds to the temporal fluctuations in the potential flow velocity magnitude V_p. Interestingly, it can be observed that the time series of the gradient of the velocity magnitude (approximately equal to the vorticity magnitude) estimated from the two outermost probes (figure 10*b*) shows qualitative similarity with the velocity magnitude from the innermost probe and blade inflow α and w_p. Conversely, the gradient estimated from the two innermost probes shows relatively non-coherent time variation. This is possibly due to the fact that the near-blade vorticity has a significant contribution from the blade shear-layer-generated small-scale fluctuations, which do not have the apparent longer-time-scale coherence observed in the velocity magnitude signal.

The spectrum of the TE rake velocity magnitude signal at various distances from the blade elucidates the influence of the interaction of ABL turbulence with blade boundary layer turbulence (figure 11) on the near-blade flow. The inboard TE rake velocity magnitude spectra (from probes 10, 31 and 52 mm from the blade surface) are compared to the corresponding LE probe w_p spectrum, and a qualitative difference between these spectra is observed in the high-frequency region (beyond approximately 1 Hz). The slope in this region is much higher for the spectrum of the velocity magnitude from the TE rake probe nearest to the blade surface (figure 11*a*), compared with that from the LE probe w_p (which is close to $-\frac{5}{3}$), possibly due to added energy at these small scales due to blade boundary-layer-generated turbulence. The slope

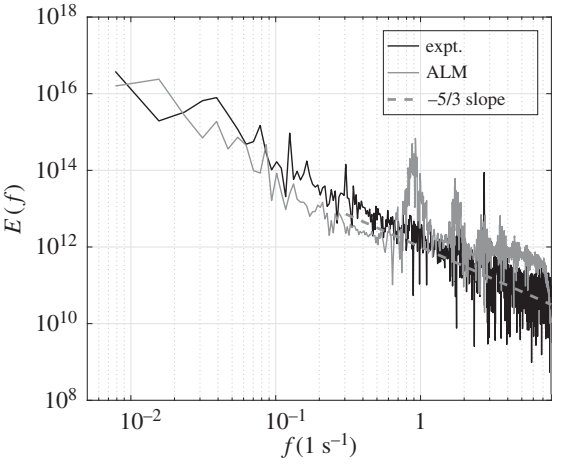

Figure 12. Comparison of the generator power spectrum from the field experiment and aerodynamic power spectrum from the ALM study. Both are from 128 s datasets.

gradually decreases with increasing distance from the blade (figure 11*b*,*c*). This is possibly due to decreasing amount of energy at these higher frequencies, which in turn is due to gradual increase in the integral length and time scales (of the blade boundary-layer-generated turbulent motions) with increasing distance from the blade surface. On the other hand, the low-frequency regions of the spectra correspond to modulations due to large eddies in the ABL, showing close correspondence with the LE probe w_p spectrum.

(d) Correlation of the integrated power to the atmospheric boundary layer inflow

Although a peak at 3P frequency (thrice per revolution) is expected in the spectrum of the 128 s long generator power data due to the combined influence of the three blades cutting through the spatially non-uniform ABL inflow, such a peak is surprisingly not observed (figure 12, black curve). Instead, the spectrum shows a strong peak near the 9P frequency, which can be possibly attributed to structural responses arising from the blades, drivetrain or the generator itself. This absence of the peak at the 3P frequency was also observed by Chamorro *et al.* [4] from their 2.5 MW wind turbine data. Contrary to the generator power behaviour, the mechanical power (solely based on aerodynamic torque) obtained from the ALM study (128 s long) shows peaks in the spectrum at 3P and its harmonics (figure 12, grey curve). At high frequencies, the spectrum of the generator power has a slope $\sim -\frac{5}{3}$. Above ≈ 1 Hz, there is concern with the accuracy of the spectrum in the ALM dataset because of the limits in the resolution at the precursor LES grid scale. Although not shown here, both the generator power from the field test and the mechanical power from the ALM study for the 128 s duration are observed to correlate well with the cup wind speed and with inflow angle α (particularly at the longer time scales), but not with the inflow angle β_p. This suggests possible influence of ABL turbulence on time variations in power, through its direct influence on α as discussed in §5a.

Data from the cup anemometer are used to quantify the influence of atmospheric turbulence on the generator power at various time scales. Figure 13*a* shows the time series of wind speed and generator power for the 128 s analysis period. Good correspondence between the signals can be observed at the 'large' time scales when the ≈ 28 s time lag for an ABL eddy to advect from the met. tower to the wind turbine rotor plane is taken into account. To understand the scale-specific modulation of the generator power by the broad-spectrum incoming ABL flow, the maximum of the time-lagged correlation coefficient between these two datasets is calculated for different frequency bands. Both signals are reconstructed using band-pass filtering allowing

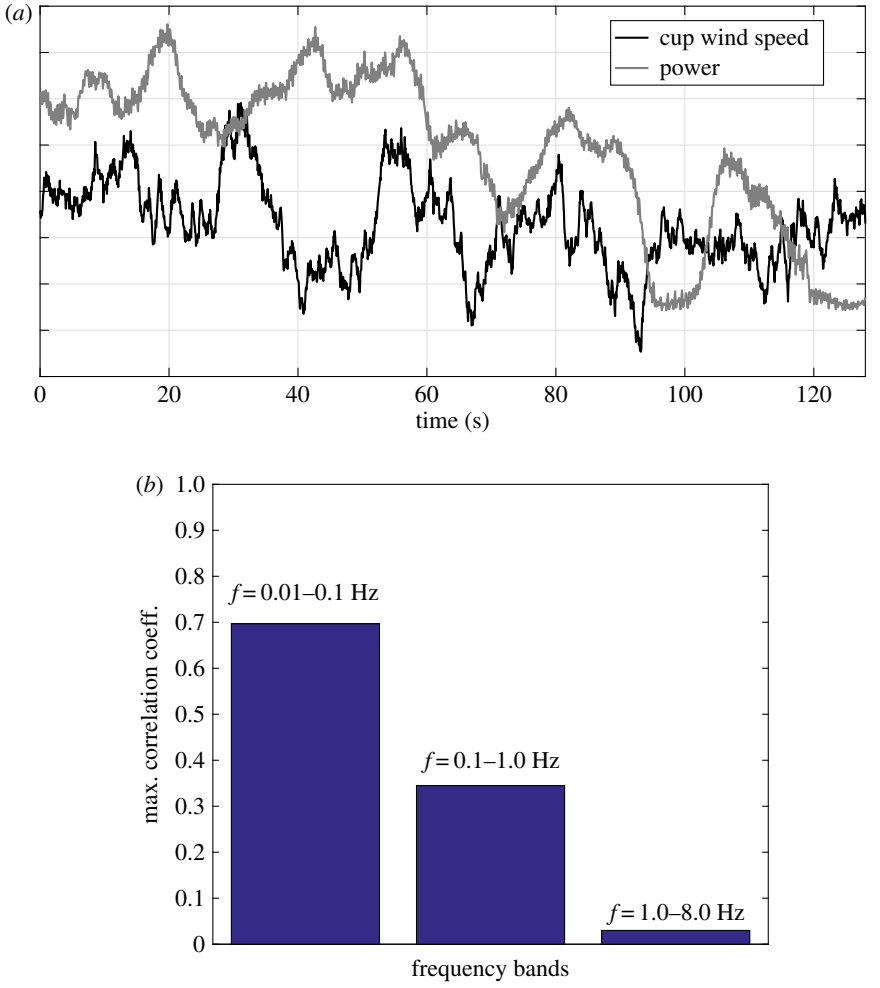

Figure 13. (*a*) Time variation of cup wind speed and generator power. The vertical axis scale is suppressed for proprietary reasons. (*b*) Scale specific correlation coefficient of band-pass filtered generator power and cup wind speed. Note that, because the 3P rotor frequency (relevant to the power data) is close to 1 Hz, the plot can be interpreted also as if frequency were non-dimensionalized with the 3P frequency. (Online version in colour.)

different ranges of frequency up to 8 Hz. In figure 13*b*, the spectra are split into three contiguous bands, each representing one decade, 0.01–0.1 Hz, 0.1–1.0 Hz and 1.0–8.0 Hz, and the maximum of the time-shifted correlation coefficient between the filtered generator power signal and cup wind speed for each of these bands is shown. It can be observed that, while there is appreciable correlation between the wind speed and the generator power in the low-frequency band (less than 0.1 Hz, i.e. time scales more than 10 s), the correlation drops drastically at higher frequencies (figure 13*b*). The maximum correlation is observed for the frequency range corresponding to the time scales of the same order of magnitude as the integral time scale estimate for the large-scale ABL horizontal motions ($\tau_{l,uu} \approx 50$ s, see §3c). Hence, there is a strong response of the time variations in generator power to atmospheric turbulent wind variations at the relatively large time scales associated with the advection of energy-containing atmospheric eddies (consistent with [4]), whereas the generator power responds relatively weakly to the higher-frequency fluctuations associated with blade passage through smaller-scale turbulence structures. Weak correlation is found to exist surrounding the 3P frequency.

6. Summary and conclusion

Using combinations of a unique dataset collected from a GE 1.5 MW wind turbine in the field during the daytime with data from an LES of an equivalent atmospheric boundary layer with an actuator-line-modelled rotor embedded within, we have analysed non-steady characteristics of the local velocity field and power of the GE 1.5 MW wind turbine in response to the passage of daytime turbulence eddies. The GE dataset is unique and particularly valuable in that it quantifies local time-varying velocity vectors relative to the leading edge and velocity magnitude through the boundary layer at the trailing edge at three locations on the outer 30% of the wind turbine blade as it rotates through the turbulence eddies of the daytime ABL. These data were collected in combination with time-synchronized generator electrical power, rotor r.p.m. and yaw, and blade pitch from a high-frequency SCADA system, as well as time-resolved meteorological data from a met. tower located 250 m upwind.

Our data analyses centre on a period of time that was chosen from the entirety of the data collected to satisfy a large number of constraints. These constraints are both in the state of the atmospheric conditions and in the time-dependent behaviour of the wind turbine rotor. Specifically, so that we could replicate the true ABL that interacts with the wind turbine as closely as possible with an LES of a corresponding dry-air ABL in equilibrium, it was necessary that the field data were collected during a period when the ABL could be reasonably well approximated as quasi-steady with no precipitation and minimal cloud cover over the course of the day. The best approximation of quasi-steadiness occurs typically over a 2–3 h period in the early afternoon, when the capping inversion is at its apogee. We are further restricted to periods where blade r.p.m. and pitch were relatively constant, with constant yaw for the planned numerical simulations. Only two short time periods satisfied the entirety of our criteria. We chose the day with the more extended period for analysis, a 128 s early afternoon period in late summer.

Using the data from the met. tower in combination with radiosonde data from a nearby airport, we produced a reasonable estimate for the ABL stability state around the analysis period. We then generated a highly resolved ABL field using a pseudo-spectral LES code, with the estimated stability state ($-z_i/L \approx 7.7$) and ABL depth ($z_i \approx 1.8$ km). Within the numerically generated ABL, a wind turbine location was chosen based on an optimal match between the met. tower and LES velocity datasets surrounding the period of analysis. ABL data at a vertical plane were extracted as time-varying Dirichlet boundary condition for a computational domain with the rotor modelled using an advanced actuator line model of the GE 1.5 MW rotor at the same pitch, r.p.m. and hub-height wind speed as during the experimental analysis period. In this way, we generated a simulation that well approximated the field campaign during the period of analysis.

Analysis of the combined experimental–numerical datasets shows clearly the existence of three dominant time scales in the aerodynamic response of the rotating wind turbine blades to the passage of energy-containing atmospheric eddies. These suggest three different time-scale responses in the forces generated on the wind turbine blades and on the moments generated at the rotor hub as a result of the passage of the coherent motions in the lower part of the ABL (also known as the surface layer). Mean shear in the surface layer causes the streamwise coherence scale in the streamwise fluctuating velocity to elongate in the streamwise direction relative to the lateral coherence scale, which grows proportionally with distance from the ground along with the characteristic horizontal scale of vertical fluctuations. Using radiosonde data from a nearby airport, we have estimated the ABL depth at 1800 m, indicating a surface layer depth that is well above the ≈ 120 m height of the GE wind turbine. These surface layer eddies manifest themselves as spatial and temporal non-uniformity in the wind turbine inflow, and figure 5 clearly shows such spatial variations having length scales comparable to the blade radius.

As the blade chord is everywhere at least an order of magnitude smaller in scale than the atmospheric eddy scale, and as the wind turbine blades rotate through the turbulence eddies, the forcing external to the blade boundary layer is expected to be roughly uniform from the leading to the trailing edge. Furthermore, given the comparable blade length to eddy scale, one may anticipate load response to the passage of the blade through atmospheric eddies to be

relatively correlated over large percentages of the blade surface, depending on the time-varying asymmetrical relationship between the rotor and eddies passing through the rotor disc. The measurements from the GE field campaign show that the time responses in local velocity at the leading and trailing edges are qualitatively similar, consistent with the above discussion (figures 6 and 10, respectively). Also, the local velocity along the outer 30% of the blade span shows very similar responses in time as the blade rotates through a coherent eddying motion in atmospheric turbulent velocity variation (not shown).

However, there are some interesting differences in time response related to specific characteristics of the velocity vector that are relevant to the nature of the forcing of the blade loads. In particular, whereas all variables display a 1P response at the blade rotation frequency, there is a higher-frequency response that is fundamentally different in two groupings of characteristics of the fluctuating velocity vector relative to the leading edge. For example, the temporal variations in flow angle in the plane of local aerofoil sections (α) have important differences from the fluctuations in the direction of the blade span (β_p). Whereas α fluctuations are likely indicative of fluctuations in aerofoil sectional loading coefficients, β_p fluctuations quantify deviations from local two-dimensional flow in response to blade rotation. The data show that β_p has a well-defined harmonic 1P response, with lower-level modulations by higher-frequency fluctuations (figure 6*b*), that appears in the frequency spectrum as a relatively narrow peak (figure 7*b*). The fluctuations in α create a 1P peak in its frequency spectrum with a much broader distribution of frequency responses surrounding the peak (figure 7*a*).

From the time domain we find that this broadening of the 1P peak of α is a result of the intermittent breaking of the 1P response that is well defined at all times in the temporal fluctuations of the spanwise angle of the local velocity vector, β_p (figure 6). The observation that the component of the leading-edge velocity vector that is roughly perpendicular to the rotor plane (w_p) fluctuates almost exactly like α, with intermittent 1P response between high-frequency relatively non-oscillatory periods (figure 6*a*), while velocity magnitude V_p (and u_p) fluctuates similarly to β_p, is a strong indication that the flow angle α is directly forced by the horizontal fluctuations in the atmospheric wind as the blade cuts through the internal structure of the atmospheric eddy, while the radial motions are only indirectly forced by the internal eddy structure. The observation that the response is highly correlated over the span of the blade (over which data are available) suggests that these same response characteristics may also be anticipated for the rotor moments that act at the hub on the low-speed shaft: torque and out-of-plane bending moment. A related blade boundary-layer-resolved simulation of the NREL 5 MW wind turbine blade rotating through daytime atmospheric boundary layer eddies [2] confirms this statement and indicates that the sub-1P time scale load responses are often highly ramp-like with large peak-to-peak variations that have the potential to pass impulse-like fluctuations in moment along the low-speed shaft, which could contribute to drivetrain component failures.

Comparison of the response in the velocity vector upwind of the leading edge of the blade with that of the velocity magnitude in the trailing-edge blade boundary layer leads to additional interesting observations. Note in particular (figure 10*a*) that the velocity magnitude fluctuations in the outer margins of the trailing-edge boundary layer contain a clear 1P characteristic very much like the velocity magnitude V_p (as well as chordwise velocity u_p) at the leading edge of the blade section. This coupled leading–trailing-edge oscillatory response is consistent with the observation made earlier that the blade chords are at least an order of magnitude smaller in scale than the coherence length of the turbulence eddies through which the blade rotates. However, the velocity fluctuations deep within the boundary layer have characteristics nearly identical to the fluctuations in α (and w_p) at the leading edge, confirmed by direct comparison of the lower time series in figure 10*a* with figure 6*a*. This observation indicates that, whereas temporal fluctuations in the nearly irrotational flow outside (or in the outer part of) the blade boundary layer are directly correlated with the temporal fluctuations in the potential flow velocity magnitude V_p at the leading edge of the corresponding blade section, the temporal fluctuations within the rotational depths of the boundary layer flow reflect instead

the fluctuations in aerofoil sectional loading that are driven by the temporal fluctuations in flow sectional flow angle α (and hence w_p). In contrast, the vorticity content of the outer boundary layer (figure 10*b*) responds similarly, with similar time scales, to the near-surface velocity field, while near the surface the vorticity is driven by the much higher frequencies of the near-surface viscid–inviscid dynamics. These blade boundary-layer-induced fluctuations generate high-frequency turbulent kinetic energy, elevating the high-frequency variance content of the spectra (figure 11*a*).

In contrast with the important differences discussed above in blade aerodynamic response at the blade rotational and sub-rotational time scales, the largest-time-scale response, reflecting advection of energy-dominant atmospheric eddies through the rotor plane, is observed consistently in the frequency spectra of all data collected at the leading and trailing edges in both the experimental and computational datasets. Indeed, all data suggest strong modulations at the large-eddy advection time scale. The spectrum of fluctuating generator power also indicates that the strong modulations in generator power are correlated with the large variations in wind speed at the large-eddy passage time scale (figure 13). However, the higher-frequency response in mechanical power at the 3P blade passing frequency is not apparent in the generator power spectrum and has relatively low correlation with the wind fluctuations, suggesting that the higher-frequency content of the mechanical power at the rotor hub may be modified as it is passed through the drivetrain to the generator.

Authors' contributions. A.H. provided the data for the field study and provided insight on the details of the instrumentation. All authors performed the data analysis of the field test. T.N.N. performed the numerical studies, and drafted the manuscript. J.G.B. and T.N.N. performed the analysis of the numerical studies. All authors contributed to the writing and final approval of the manuscript.

Competing interests. We declare we have no competing interests.

Funding. We are grateful for primary financial support from the US Department of Energy's Office of Energy Efficiency and Renewable Energy (EERE). We are also grateful for additional support from the Penn State Applied Research Laboratory, the Penn State Cyber Science Institute (CSI), the Penn State Institutes of Energy and the Environment (PSIEE) and the Penn State Departments of Aerospace Engineering, and Mechanical and Nuclear Engineering.

Acknowledgements. In addition to support from the DOE's EERE and the Penn State PSIEE, CSI and Departments of Aerospace and Mechanical Engineering, we acknowledge a very high level of computational support from the NSF XSEDE program (specifically the Pittsburg Supercomputing Center (PSC) and the Texas Advanced Computing Center (TACC)). We are specifically grateful for expert technical help from Dr Anirban Jana of the PSC. We have also received significant computer support from the DOE Oak Ridge Leadership Computing Facility (LCF) and the NREL Peregrine facility. We are very grateful to our colleagues at GE Global Research in Munich, Germany, who have been very helpful and supportive. In particular, we acknowledge much internal support from and discussion with Dr Dominic Von Terzi. Dr Stefan Kern was involved in discussion and with the organization of the data. In regards the latter, we also acknowledge Dr Kevin Kinzie of GE Energy. We are very grateful to Dr Peter Sullivan of the National Center for Atmospheric Research (NCAR) for allowing us to use his highly parallelized atmospheric boundary layer code ([17]). We also acknowledge valuable discussions with Drs Scott Schreck and Matthew Churchfield of the NREL National Wind Technology Center.

References

1. Khanna S, Brasseur JG. 1998 Three-dimensional buoyancy- and shear-induced local structure of the atmospheric boundary-layer. *J. Atmos. Sci.* **55**, 710–743. (doi:10.1175/1520-0469(1998)055<0710:TDBASI>2.0.CO;2)
2. Vijayakumar G, Brasseur JG, Lavely AW, Jayaraman B, Craven B. 2016 Interaction of atmospheric turbulence with blade boundary layer dynamics on a 5 MW wind turbine using blade-boundary-layer-resolved CFD with hybrid URANS-LES. In *34th Wind Energy Symposium, AIAA SciTech*, San Diego, CA, USA, AIAA Paper 2016-0521.
3. Kelley ND. 1994 Turbulence descriptors for scaling fatigue loading spectra of wind turbine structural components. NREL/TP–442-7035. National Renewable Energy Lab., Golden, CO, USA.

4. Chamorro LP, Lee SJ, Olsen D, Milliren C, Marr J, Arndt RE, Sotiropoulos F. 2015 Turbulence effects on a full-scale 2.5 MW horizontal-axis wind turbine under neutrally stratified conditions. *Wind Energy* **18**, 339–349. (doi:10.1002/we.1700)
5. Tobin N, Zhu H, Chamorro LP. 2015 Spectral behaviour of the turbulence-driven power fluctuations of wind turbines. *J. Turbul.* **16**, 832–846. (doi:10.1080/14685248.2015.1031242)
6. Madsen HA *et al.* 2010 The DAN-AERO MW Experiments—Final report. Riso-R-1726 (EN).
7. Medina P, Singh M, Johansen J, Jove A, Fingersh L, Schreck S. 2012 Inflow characterization and aerodynamics measurements on a SWT-2.3-101 wind turbine. In *50th AIAA Aerospace Sciences Meeting, Nashville, TN, USA*, AIAA Paper 2012-0230.
8. Link H, Keller J, Guo Y, McNiff B. 2013 Gearbox Reliability Collaborative Phase 3 Gearbox 2 test plan. NREL/TP-5000-58190. National Renewable Energy Lab. (NREL), Golden, CO, USA.
9. Crowther A, Ramakrishnan V, Zaidi NA, Halse C. 2011 Sources of time-varying contact stress and misalignments in wind turbine planetary sets. *Wind Energy* **14**, 637–651. (doi:10.1002/we.447)
10. Ionescu L, Pontius T. 2009 Main shaft support for wind turbine with as fixed and floating bearing configuration. Technical Paper, The Timkin Company.
11. Churchfield MJ, Lee S, Michalakes J, Moriarty PJ. 2012 A numerical study of the effects of atmospheric and wake turbulence on wind turbine dynamics. *J. Turbul.* **13**, 1–32. (doi:10.1080/14685248.2011.633522)
12. Jha PK, Schmitz S. 2016 Blade load unsteadiness and turbulence statistics in an actuator-line computed turbine–turbine interaction problem. *J. Solar Energy Eng.* **138**, 031002. (doi:10.1115/1.4032545)
13. Wyngaard JC. 2010 *Turbulence in the atmosphere*. Cambridge, UK: Cambridge University Press.
14. Khanna S, Brasseur KG. 1997 Analysis of Monin–Obukhov similarity from large-eddy simulation. *J. Fluid Mech.* **34**, 251–286. (doi:10.1017/S0022112097006277)
15. Jha PK, Churchfield MJ, Moriarty PJ, Schmitz S. 2014 Guidelines for volume force distributions within actuator line modeling of wind turbines on large-eddy simulation-type grids. *J. Solar Energy Eng.* **136**, 031003. (doi:10.1115/1.4026252)
16. Vijayakumar G, Lavely AW, Jayaraman B, Craven B, Brasseur JG. 2014 Blade boundary layer response to atmospheric boundary layer turbulence on a NREL 5 MW wind turbine blade with hybrid URANS-LES. In *32nd ASME Wind Energy Symposium*, National Harbor, MD, USA, AIAA Paper 2014-0867.
17. Sullivan PP, Patton EG. 2011 The effect of mesh resolution on convective boundary layer statistics and structures generated by large-eddy simulation. *J. Atmos. Sci.* **68**, 2395–2415. (doi:10.1175/JAS-D-10-05010.1)
18. Moeng CH. 1984 A large-eddy-simulation model for the study of planetary boundary-layer turbulence. *J. Atmos. Sci.* **41**, 2052–2062. (doi:10.1175/1520-0469(1984)041<2052:ALESMF>2.0.CO;2)
19. Vijayakumar G, Brasseur JG, Lavely AW, Kinzel MP, Paterson EG, Churchfield MJ, Moriarty PJ. 2012 Considerations in coupling LES of the atmosphere to CFD around wind turbines. In *50th AIAA Aerospace Sciences Meeting, Nashville, TN, USA*, AIAA Paper 2012-0817.
20. OpenFOAM. ESI Group. See www.http://openfoam.org/.
21. Sorensen JN, Shen WZ. 2002 Numerical modeling of wind turbine wakes. *J. Fluids Eng.* **124**, 393–399. (doi:10.1115/1.1471361)
22. Troldborg N. 2008 Actuator line modeling of wind turbine wakes. PhD thesis, Technical University of Denmark, Lyngby, Denmark.
23. Connell JR. 1982 The spectrum of wind speed fluctuations encountered by a rotating blade of a wind energy conversion system. *Solar Energy* **29**, 363–375. (doi:10.1016/0038-092X(82)90072-X)